PAPER

A thermoresponsive liquid with unique two-way volume memory function

To cite this article: Mingzhe Li et al 2021 Smart Mater. Struct. 30 055018

View the <u>article online</u> for updates and enhancements.

Smart Mater. Struct. 30 (2021) 055018 (9pp)

https://doi.org/10.1088/1361-665X/abf41e

A thermoresponsive liquid with unique two-way volume memory function

Mingzhe Li, Chi Zhan and Weiyi Lu*

Department of Civil and Environmental Engineering, Michigan State University, East Lansing, MI 48824, United States of America

E-mail: wylu@egr.msu.edu

Received 30 October 2020, revised 8 March 2021 Accepted for publication 31 March 2021 Published 20 April 2021



Abstract

Shape memory materials (SMMs) recover their original shape as an external stimulus is applied. To meet the growing needs for complicated applications, it is imperative to design advanced SMMs with more functions and better performance. This paper reports a new design of liquid-based SMMs, i.e. liquid nanofoam (LN) system, by controlling the extent of liquid outflow from hydrophobic nanopores. The liquid outflow behavior is dominated by the thermoresponsive sensitive bubble nucleation process in the confined nanoenvironment. As temperature increases, the extent of liquid outflow is promoted, and the system volume is recovered. Thus, the LN system exhibits an instant volume memory behavior. As temperature decreases, the volume memory behavior is reversed. A constitutive model for the shape memory LN material has also been developed and validated. The thermoresponsive nanoconfined liquid outflow opens up new avenues for the design of advanced SMM.

Keywords: liquid nanofoam, shape memory material, thermoresponsive, liquid outflow, bubble nucleation

(Some figures may appear in colour only in the online journal)

1. Introduction

Shape memory materials (SMMs) are smart and adaptive materials that are capable of recovering their original shapes from a plastic deformation in response to an external stimulus [1–3]. The external stimulus includes temperature [4, 5], light [6, 7], pH [8, 9], and electric [10, 11] and magnetic [12, 13] fields. The stimulus responsive properties have made SMMs promising for various applications such as actuators [14, 15], sensors [16], microfluidics [17], and many others.

Over the past decades, various SMMs have been developed, among which shape memory alloys (SMAs) [3, 18, 19] and shape memory polymers (SMPs) [6, 7, 20] are most commonly used. For instance, NiTi-based SMAs is one of the most prevalent SMAs due to their high performance and good biocompatibility. Polymeric materials, such as multidomain copolymers [21], hydrogels [22] and liquid crystalline elastomers [23], have also drawn increasingly attention as

stimuli-responsive SMPs because of their synthetic flexibility and easiness for tailoring. In addition, intensive efforts have been devoted to improving the versatility of SMMs. One-step SMMs can only remember one permanent shape [24], while multi-step SMMs can recover multiple temporary but stable shapes when exposed to a stimulus [25]. Two-way SMMs have also been designed with reversible, bidirectional shape memory function [26].

Despite these achievements in SMMs research and technology, it remains a challenge to develop SMMs with more functions and better performance to fulfill the growing demands for advanced engineering applications. To address the challenges, SMMs with new shape memory mechanisms are desired. Specially, current SMMs are mainly solid-based, while liquid-based SMMs are still scarce. It is anticipated that liquid-based SMMs are endowed with multiple advantages. Due to its intrinsic fluidity, liquid-based SMMs are more flexible and can be easily accommodated to structures with any shape and size. In addition, the hydrostatic force response of liquid-based SMMs is isotropic, which is versatile to design liquid-based smart devices.

^{*} Author to whom any correspondence should be addressed.

One strategy to develop liquid-based SMMs is to employ the reversible liquid flow in hydrophobic nanochannels [27]. As liquid molecules flow out of the nanochannels, the overall system volume is recovered. Thus, multiple memorable shapes can be engineered by controlling the extent of liquid outflow from the nanochannel by an external stimulus. Recently, a liquid nanofoam (LN) system [28–30], employing the liquid flow in hydrophobic nanopores as its deformation mechanism, is developed and could be a promising candidate for liquid-based SMMs. In this study, we have demonstrated that through precisely controlling the extent of liquid outflow from hydrophobic nanopores by temperature, LN system has shown a unique reversible and bidirectional thermoresponsive shape memory function.

2. Background

LN is a mixture of a hydrophobic nanoporous media and a liquid phase (figure 1). At ambient condition, the liquid stay outside of the nanopores due to its surface hydrophobicity. As an external force is exerted (figure 2), initially, the LN shows an elastic response ('AB'), and the system bulk modulus is the combination of the individual moduli of the liquid and solid compositions. When the internal pressure reaches a critical value (point 'B'), the energy barrier caused by the hydrophobic surface is overcome and the liquid molecules are driven into the nanopores. As a result, the slope of the curve decreases, and an infiltration plateau ('BD') is formed. The critical pressure at which liquid molecules start to infiltrate into the nanopores is defined as the liquid infiltration pressure, $P_{\rm in}$, which is governed by the classic Laplace-Young equation, $P_{\rm in} = 2\Delta \gamma/r$, where $\Delta \gamma$ is the excessive solid–liquid interfacial tension and r is the nanopore radius. As all the nanopores are filled with liquid molecules, the infiltration plateau ends, and the LN system becomes elastic again ('DE'). The width of the infiltration plateau, $\Delta\omega$, is determined by the nanopore volume of the LN system. Thanks to the ultra-fast liquid flow in hydrophobic nanopores, this mechanical response of LN system is insensitive to external loading speed, from quasi-static to intermediate strain rates [31].

As the external force is removed, the pressure drops abruptly ('EF'), followed by a much-reduced slope of the unloading curve ('FG'). The reduced slope as well as the associated system volume recovery reveal the liquid and gas outflow from the hydrophobic nanopores [32]. It has been demonstrated that the extent of liquid outflow from nanopores is dominated by the bubble nucleation process [33–35]. In a gas-containing LN system, the gas molecules are dissolved in the liquid phase during the liquid infiltration process. Upon unloading, the dissolved gas molecules may become supersaturated and tend to escape from the liquid phase to the vapor phase. Meanwhile, the liquid phase flows out from the hydrophobic nanopores. It has also been found that the bubble nucleation process is highly sensitive to temperature [36–38]. At elevated temperature, the bubble nucleation is more prone to occur, leading to a promoted extent of liquid outflow from hydrophobic nanopores. Therefore, at extreme

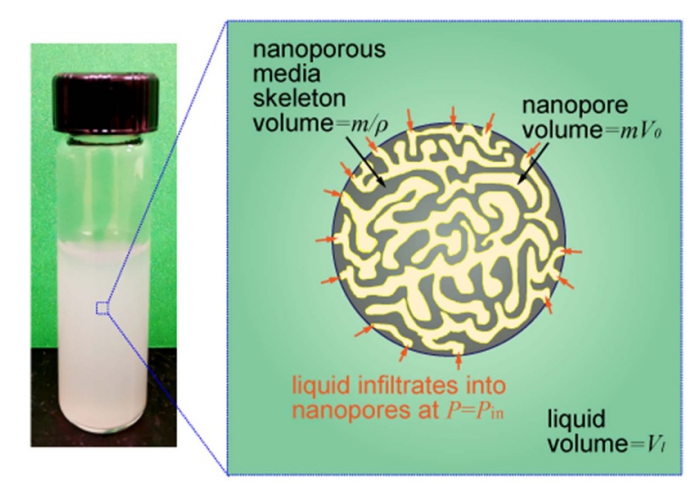


Figure 1. (a) A typical LN sample (b) simplified model for a shape memory LN sample.

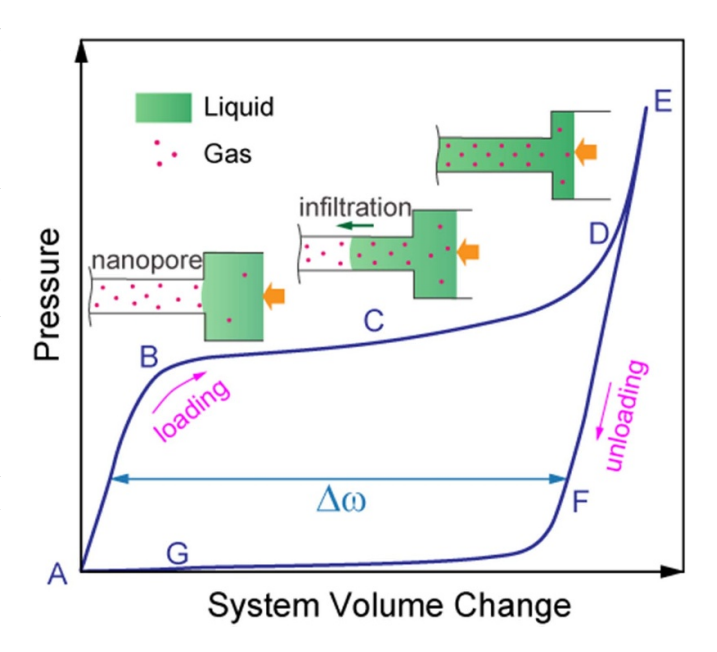


Figure 2. Typical mechanical response of LN in the first loading–unloading cycle.

low temperature, the bubble nucleation process does not occur, and the liquid phase is 'locked' in the hydrophobic nanopores, resulting in a smaller compressibility in the subsequent loading cycles (figure 3(a)). At relatively high temperature, the gas molecules are separated from the liquid phase and the liquid molecules are fully repelled from the hydrophobic nanopores. Consequently, the system will show a fully preserved compressibility in the subsequent loading cycles (figure 3(b)).

As depicted in figure 1, an LN system is composed of a hydrophobic nanoporous media with the mass of m and a liquid phase with the volume of V_1 . The specific pore volume of the hydrophobic nanoporous media, i.e. the specific volume of gas at ambient condition, is V_0 . Given these system compositions, the volume of nanoporous media skeleton is m/ρ , where ρ is the density of the skeleton material. For amorphous solid silica, $\rho = 2.2$ g cm⁻³. The volume of the nanopores is mV_0 .

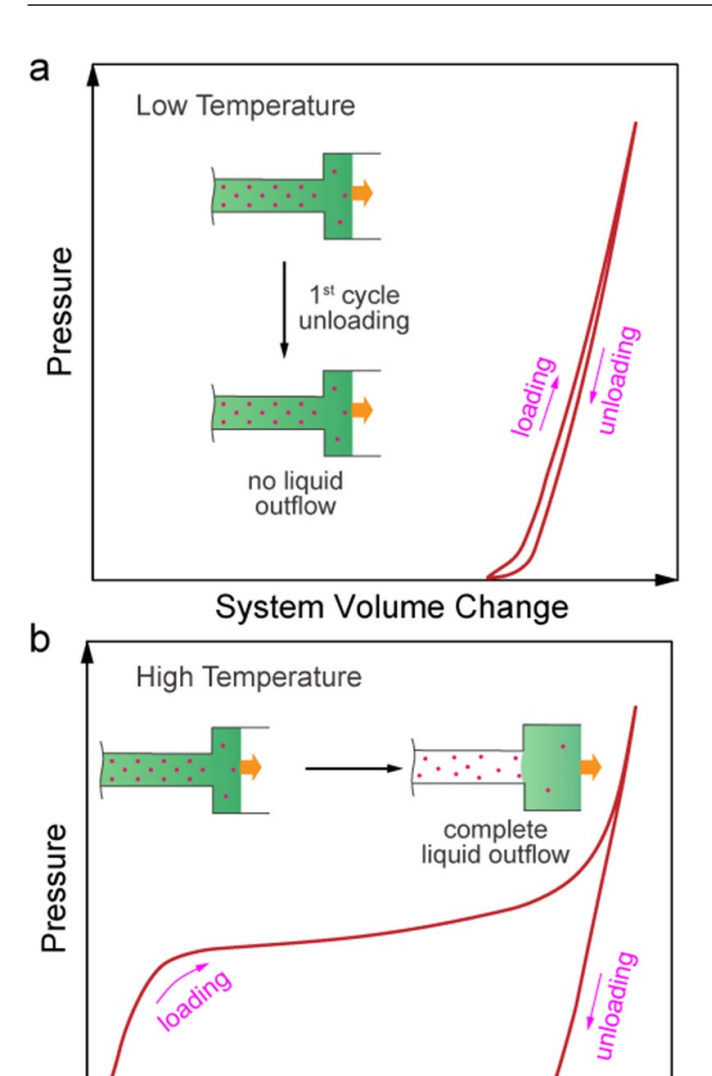


Figure 3. Typical mechanical response of LN in all subsequent loading–unloading cycles (a) at low temperature (b) at high temperature.

System Volume Change

The total system volume is $mV_0 + m/\rho + V_l$. Thus, at extreme low temperature, the system has no compressibility and the plastic system volume change, $\Delta\omega$, is nearly zero. While at relatively high temperature, $\Delta\omega$ is

$$\Delta\omega = \frac{mV_0}{mV_0 + m/\rho + V_l}. (1)$$

3. Materials and methods

3.1. Materials

A hydrophilic nanoporous silica gel (SP-120-10, DAISO Fine Chem USA, Inc.) was used as the nanoporous media in the LN in current study. The as-received material was in powder form, with an average particle size around 10 μ m and pore size of 12 nm. The specific pore volume of the silica gel

 V_0 was around 0.6 cm³ g⁻¹. To make its nanopore surface hydrophobic, a monolayer of n-octyldimethylchlorosilane was anchored onto its surface. The detailed description can be found in [29, 31]. Briefly, about 1 g of nanoporous silica was mixed with 40 ml of anhydrous toluene for 3 h at 90 °C. Ten milliliter of n-octyldimethylchlorosilane and 1 ml of pyridine were injected into the mixture at room temperature. The mixture was then stirred at 95 °C for 24 h, after which the surface-modified nanoporous silica was filtered, rinsed by ethanol, and dried for at least 24 h.

The liquid phase of the LN was 25 wt.% lithium chloride (LiCl) aqueous solution. The freezing point of the LiCl solution was lower than -70 °C [39], which fulfilled typical industrial standards of operating temperatures [40].

The LN sample was prepared by mixing 0.2 g of surface-modified nanoporous silica and 0.4 ml of 25 wt.% LiCl aqueous solution in a testing cell with two O-ring equipped pistons. The LN sample was pre-compressed to minimize the air trapped in between the nanoporous silica particles, as detailed in our previous work [28, 32]. The cross-sectional area of the pistons, *A*, was 126 mm².

3.2. Characterization of thermo-mechanical properties of LN

LN sample sealed in the testing cell was compressed by a universal tester (Floor Model 5982, Instron, Inc.) equipped with environmental chamber (Table Model 3119-609, Instron, Inc.) at system temperature T=-60, -45, -30, -15, 0, 25, and 90 °C. The loading speed was 2 mm min⁻¹ (strain rate = $6.7 \times 10^{-3} \text{ s}^{-1}$). The applied force, F, gradually increased to 6 kN, leading to an equivalent pressure of 48 MPa in the testing cell. When F reached the peak force, the crosshead of the Instron was moved back at the same speed. The loading–unloading process was repeated at least three times for each LN sample. The pressure in the testing cell was calculated as P = F/A. The system volume change of the LN sample was calculated as $\omega = \delta/l$, where δ was the measured piston displacement and l = 5 mm was the initial LN sample length for all following cyclic tests.

4. Results and discussion

4.1. Isothermal mechanical behavior of LN at various temperatures

Figure 4(a) shows typical isothermal mechanical response of LN samples in the first loading–unloading cycle at various temperatures. At T=-60 °C, the infiltration starts at $\omega=4.3\%$ and ends at $\omega=24.2\%$. The plastic system volume change $\Delta\omega$ is 19.9% and close to the theoretical value 19.6% calculated from equation (1). As the external force is removed, the LN system shows a sharp linear response until the pressure decreases to zero at $\omega=21\%$. This fast-linear reduction of LN system pressure at T=-60 °C indicates the bubble nucleation does not occur and the extent of liquid outflow is nearly zero. As the temperature gradually increases, the loading curves remain almost the same, that is, neither the infiltration pressure nor the plastic system volume change of

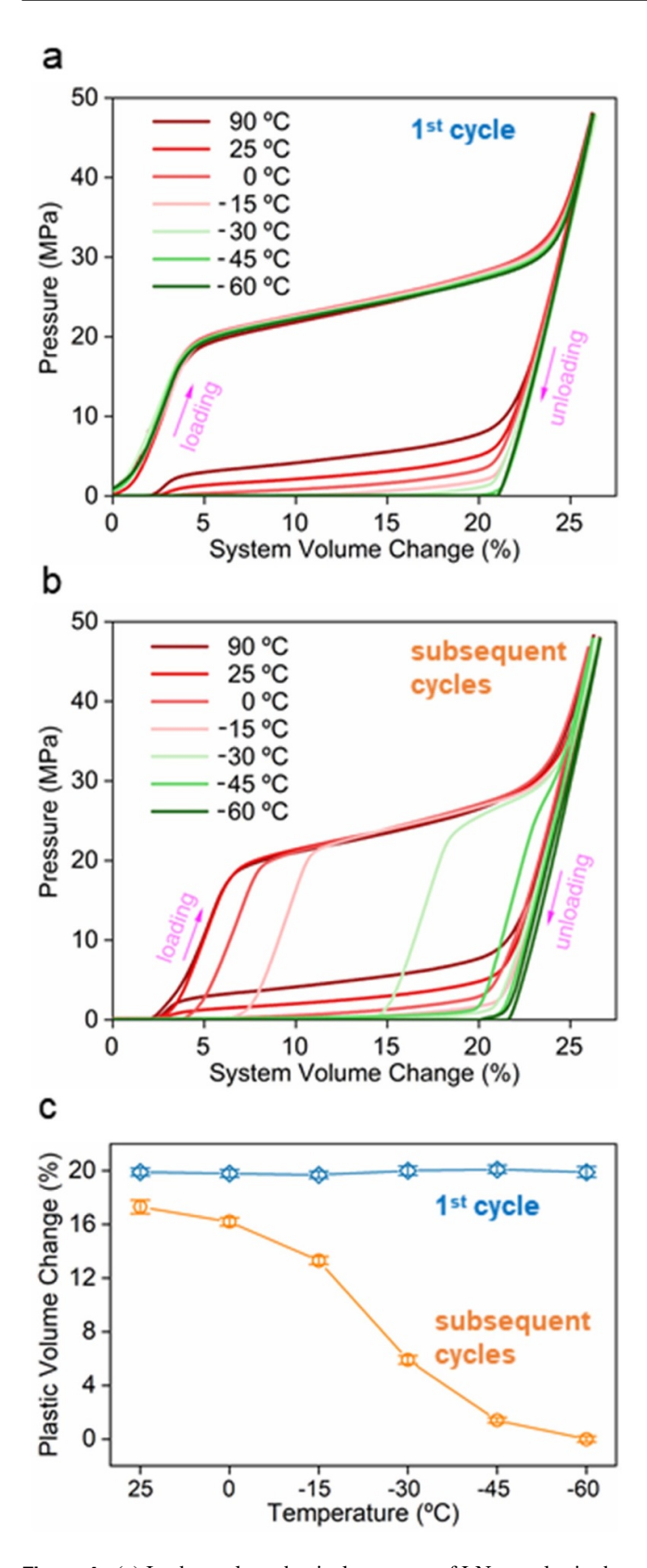


Figure 4. (a) Isothermal mechanical response of LN samples in the first loading–unloading cycle at various temperatures. (b) Isothermal mechanical response of LN samples in all the subsequent loading–unloading cycles at various temperatures. (c) The plastic volume change of LN samples at various temperatures.

the LN is affected by the elevated temperature. The nearly identical loading curves prove that the nanoporous structure of the particles is not deformed and the solid-liquid-gas interfacial tension is a constant. However, the unloading curves are extremely sensitive to temperature increase. After a linear reduction of the system pressure, a clear turning point followed by a defiltration plateau is observed. Consequently, the ending point of the unloading process is extended. To be specific, the unloading process ends at $\omega = 2.7\%$ for LN system at T = 25 °C. The thermally-sensitive unloading curve is consistent with previous studies [35, 41]. The extended defiltration plateau indicates that the liquid molecules partially or even fully flow out of the hydrophobic nanopores. As the temperature further increases from 25 °C to 90 °C, the stress level of the unloading curve increases while the ending point of unloading curve shows negligible change. Since the system recoverability may not be precisely quantified from the unloading curve in the first loading-unloading cycle, the loading curves of LN sample in the subsequent loading-unloading cycles are a direct and accurate measure.

Figure 4(b) shows typical mechanical response of LN samples in all subsequent loading-unloading cycles at various temperatures. Since all subsequent loading-unloading curves are identical to that in the second cycle, only the curves in the second cycle are shown here for clarity. For LN sample at T=-60 °C, the 'plastic' system volume change $\Delta\omega$ is zero, which agrees well with the sharp unloading curve in the first loading-unloading cycle. As temperature is elevated, the $\Delta\omega$ in the 2nd cycle of LN sample increases (figure 4(b)). At T = 25 °C, $\Delta \omega$ is promoted to 17.5%. The increased $\Delta \omega$ is due to the much-enhanced bubble nucleation process, facilitating the liquid outflow from the hydrophobic nanopores [33]. Since the liquid outflow process is completed at T=25 °C, further increasing temperature to T = 90 °C leads to nearly zero variation of $\Delta\omega$. Please note that from the second loadingunloading cycle, the LN system becomes fully reusable at specified temperature and volume memorable as temperature changes.

4.2. Volume memory behavior of LN in heating

LN sample at T = -60 °C is first employed to demonstrate the volume memory behavior of LN in heating. As the unloading process in (N-1) cycle ends, the system temperature is elevated to a specified value by controlling the Instron environmental chamber. Once the temperature reaches the target value, another loading–unloading cycle N is applied on the LN sample to evaluate its volume memory behavior.

Figure 5(a) shows typical thermo-mechanical response of LN samples after heating up from -60 °C to 25 °C. Initially, the LN shows zero plastic volume change at -60 °C. Upon heating, the system volume increases gradually. As the temperature reaches 25 °C and another loading cycle is exerted. The LN exhibits a remarkable increase in the system plastic volume change. Compared with the loading–unloading curves

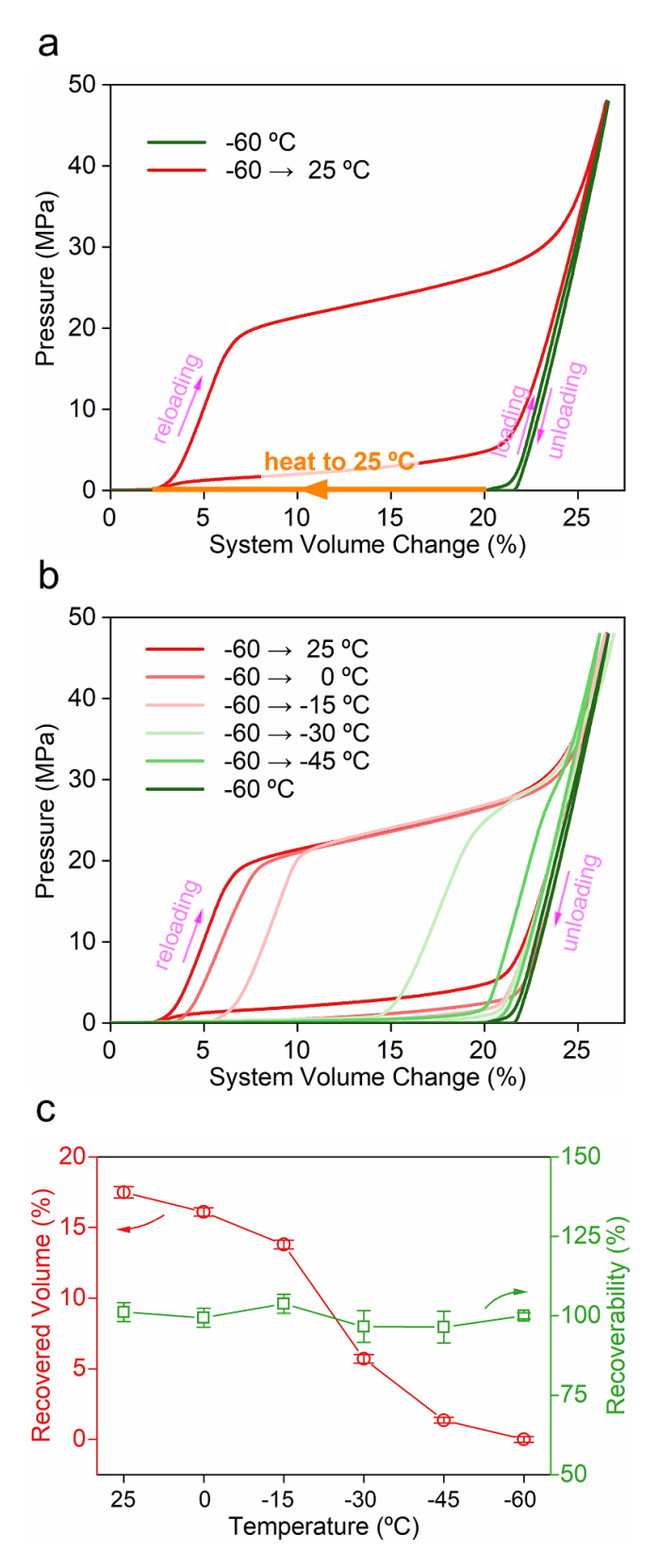


Figure 5. (a) Typical volume memory behavior of LN samples upon heating up from -60 °C to 25 °C. (b) Mechanical response of LN samples in the N cycle upon heating up to elevated temperatures after (N-1) cycle. (c) The recovered plastic volume and recoverability of LN samples in the N cycle after heating up to elevated temperatures after (N-1) cycle.

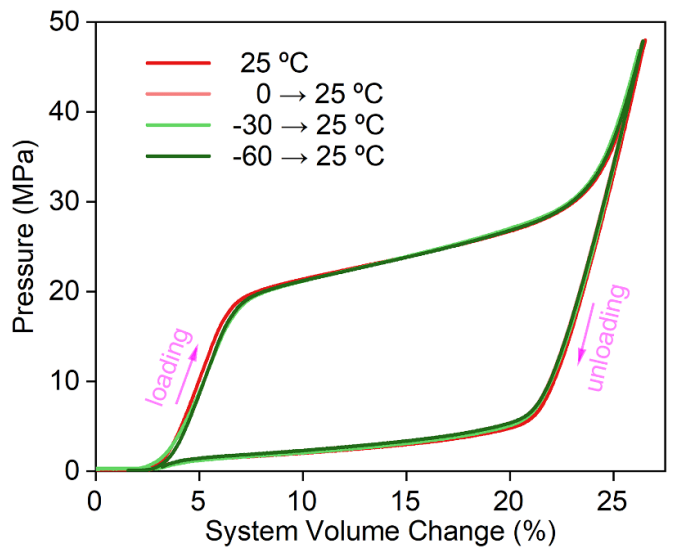


Figure 6. Mechanical response of LN samples in the N cycle upon heating up from low temperatures to 25 $^{\circ}$ C after (N-1) cycle.

at 25 °C in figure 4(b), the infiltration pressure as well as the plastic volume change are fully recovered. As shown in figure 5(b), same trends are observed when the LN is heated up to various temperatures. The recovered volume at elevated temperatures is also plotted in figure 5(c), agreeing well with the extent of liquid outflow at given temperature points shown in figure 4(c). The plastic volume change, i.e. the deformability, of the LN system is dominated by the nanopore volume in the LN and can reach 17%, which is about five times that of shape memory NiTi alloys [18, 19, 42]. The recoverability of the LN system as temperature changes can be calculated using the following equation:

$$R(T) = \frac{\Delta\omega_{T_0 \to T}}{\Delta\omega_T} \times 100\%$$
 (2)

where $\Delta\omega_T$ is the plastic system volume change at temperature T and $\Delta\omega_{T_0\to T}$ is the plastic system volume change as temperature changes from T_0 to T. As shown in figure 5(c), the recoverability R is nearly 100% at various temperatures.

Similar volume memory behavior is observed when LN samples at various low temperatures are heated up to 25 °C and shown in figure 6. As previously discussed, the volume memory behavior is attributed to the well-preserved extent of bubble nucleation and liquid outflow at different temperatures. According to the bubble nucleation theory [33, 34], the system thermodynamic equilibrium is expressed as

$$P\Delta\omega = \Delta\gamma A + P_{\sigma}V_{\sigma} \tag{3}$$

where P is the system pressure, $\Delta \gamma$ is the liquid–solid–gas interfacial tension, A is the effective surface area, $P_{\rm g}$ is the gas partial pressure, $V_{\rm g}$ is the gas volume. P, $\Delta \gamma$, and $P_{\rm g}$ are

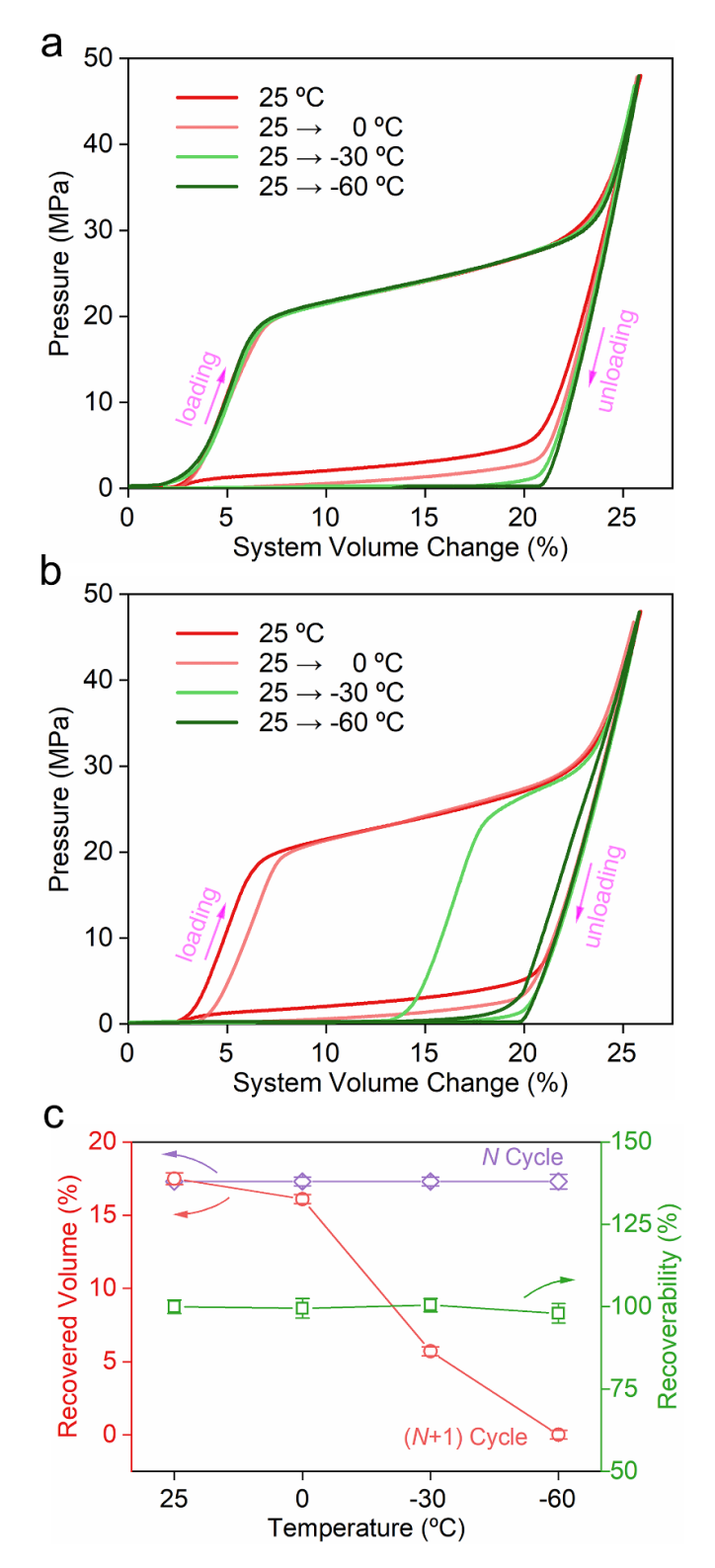


Figure 7. Upon cooling down to low temperatures after (N-1) cycle (a) mechanical response of LN samples in the N cycle. (b) Mechanical response of LN samples in the (N+1) cycle. (c) The recovered volume and recoverability of LN samples.

temperature-dependent parameters. As temperature is elevated, these temperature-dependent parameters change accordingly, leading to the target $\Delta\omega$ and rebalance of equation (3) at a given temperature.

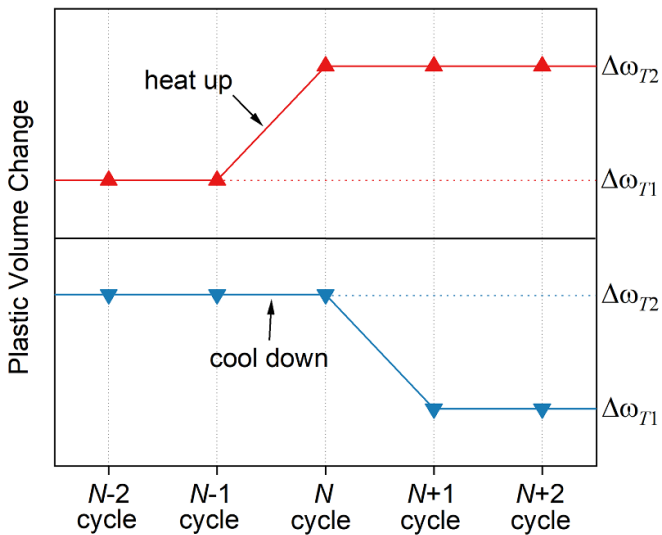


Figure 8. Instant volume memory behavior in heating and delayed volume memory behavior in cooling.

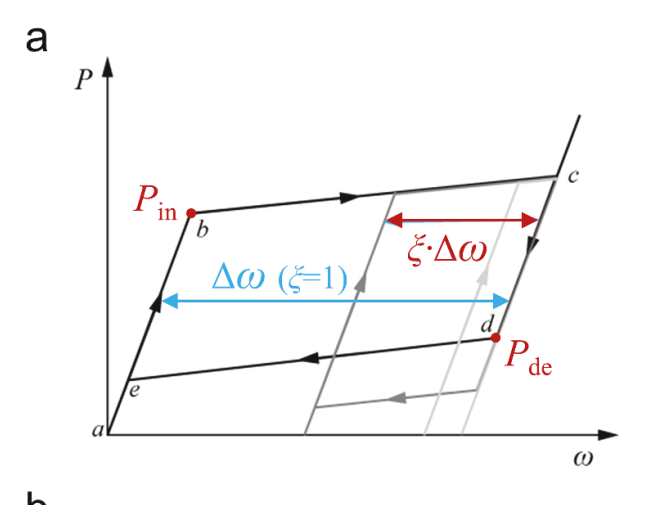
4.3. Volume memory behavior of LN in cooling

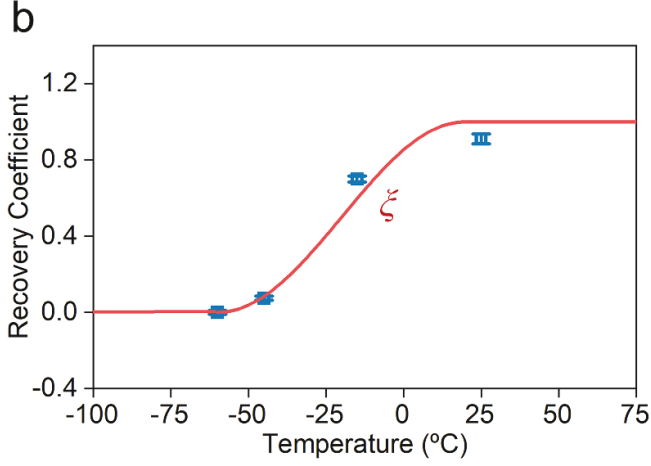
To demonstrate the volume memory behavior of LN system in cooling, LN sample with initial T=25 °C is evaluated. As the unloading process in (N-1) cycle ends, the system is cooled down to a specified temperature. Two consecutive loadingunloading cycles, namely N and (N + 1), are applied on the LN sample. Figure 7 shows typical mechanical response of LN samples in N and (N + 1) cycles after cooling down to various low temperatures. Different from the instant volume memory behavior in heating, the LN system shows a delayed volume memory in cooling. As shown in figure 7(a), the loading curves of LN after cooling down to low temperatures resemble that at 25 °C and only the unloading curves exhibit dramatic changes. For example, as temperature decreases to -60 °C, the unloading curve is similar to that in figure 4, indicating no plastic volume is recovered during the unloading process. As expected, the nearly 100% volume memory ability is observed in the (N + 1) cycle (figures 7(b) and (c)).

This delayed volume memory behavior is due to the liquid-gas interaction in the hydrophobic nanopores. In heating cases, the bubble nucleation, which reduces the system free energy, is a spontaneous process. Therefore, upon heating, bubble nucleation as well as liquid outflow occur immediately, and the plastic system volume change is recovered (figure 8). However, in cooling cases, the gas dissolution, which is the reverse process of bubble nucleation, requires external loading to occur. Thereafter, the volume memory behavior is activated in the (N+1) loading process (figure 8).

4.4. Constitutive model for the shape memory behavior of LN material

This section presents a constitutive model based on phenomenological aspects of thermomechanical behavior of the LN shape memory material by following the SMA one [43]. In





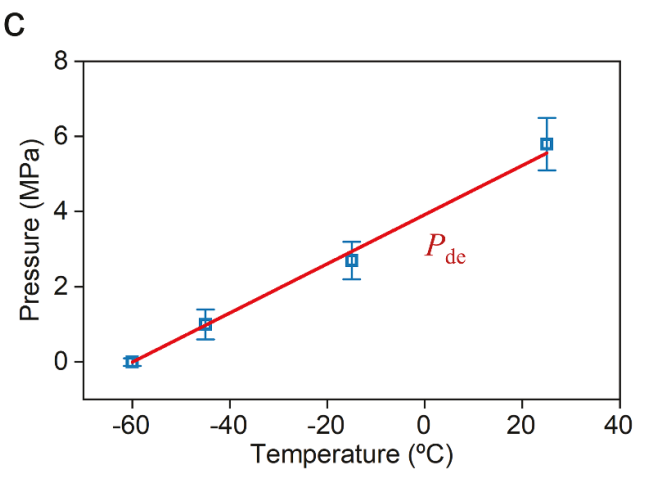


Figure 9. (a) Proposed constitutive model for LN shape memory material. (b) Recovery coefficient for the LN shape memory material. (c) The initial recovery pressure which is the pressure at the turning point of the unloading curve.

this model, the constitutive relationship for pressure is written as

$$P - P^{0} = K \ \omega - \omega^{0} \left(-K\Delta\omega \ \xi - \xi^{0} \right)$$
 (4)

where K is the bulk modulus of the material, ω is the volumetric strain of the material, $\Delta\omega$ is the plastic volumetric strain at complete recovery, and ξ is the recovery extent of the material.

Table 1. Computations associated with the volume memory effect.

| | P | ω |
|-----------------------------|---|---------------------------|
| a | 0 | $(1-\xi)\Delta\omega$ |
| $\mathbf{a} \to \mathbf{b}$ | $P = K[\omega - (1 - \xi) \Delta \omega]$ | |
| b | $P_{a \to b} = P_{b \to c}$ | |
| $b \to c$ | $P = K_m \omega + P_1$ | |
| c | $P_{b \to c} = P_{c \to d}$ | |
| $c \to d$ | $P = K(\omega - \Delta\omega)$ | |
| d | P_{de} | $P_{de}/K + \Delta\omega$ |
| $d \to e $ | $P = P_{de} + K_n \omega - P_2$ | |

Table 2. Material parameters in the constitutive model.

| K | 580 MPa |
|-------|---------|
| P_1 | 16 MPa |
| K_m | 54 MPa |
| K_n | 35 MPa |
| P_2 | 7.3 MPa |
| | |

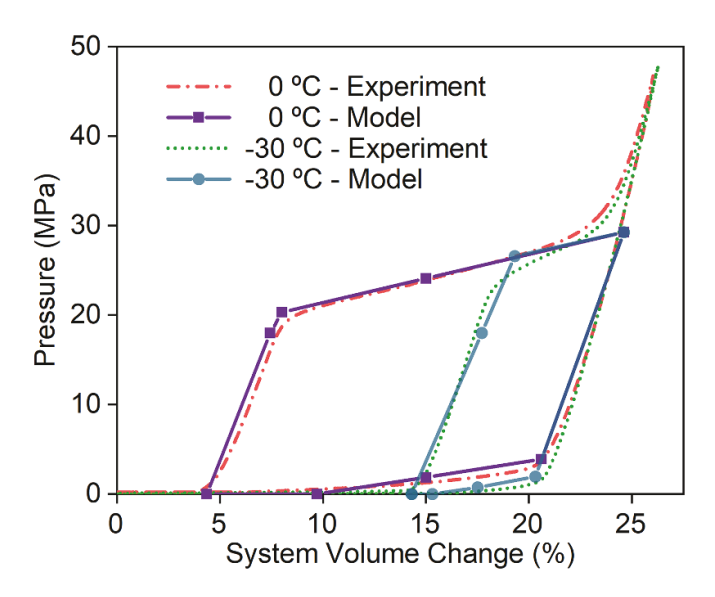


Figure 10. Comparison between numerical and experimental results.

The superscript 0 denotes the initial values of volume change and recovery extent. K is generally obtained from the pressure-volume change response of the LN material over the linear elastic regime. ξ is bounded between 0 (nearly zero recoverability at low temperature) and 1 (fully recovered) and is obtained by analyzing the hysteresis loop shown in previous experimental data. These model parameters are adjusted using the experimental results at T=25, -15, -45, and -60 °C in current study. Then, the constitutive model is validated by the experimental results obtained at T=0 and -30 °C in this study.

Figure 9(a) shows the proposed model and table 1 summarizes the formula in the model. The recovery extent is modeled with the thermodynamic function

$$\xi = \frac{1}{2} \left| \sin \right| \frac{T - T_i}{T_f - T_s} \pi - \frac{\pi}{2} \left[+1 \right]$$
 (5)

where ξ is the recovery coefficient, T_s and T_f are the initial and final recovery temperatures. $\xi = 1$ when $T > T_f$. $\xi = 0$ when $T < T_i$. T_i is set to -60 °C, at which ξ converges to 0. By fitting the above equation to the data points at T = 25, -15, -45, and -60 °C, $T_f = 20$ °C. From the linear regression analysis of the experimental data shown in figure 9(c), $P_{de} = 3.9 + 0.065T$. All other material parameters as shown in table 2 have also been obtained by fitting the formula with the experimental data at T = 25, -15, -45, and -60 °C. Thus, the constitutive model has been fully calibrated.

Figure 10 presents the predicted shape memory behavior of LN material at T=0 and -30 °C. The numerical results show good agreement with the experimental data, validating the proposed constitutive model.

5. Conclusion

In summary, we have demonstrated a novel design of liquid-based volume memory material in this work. The LN system shows a distinct two-way volume memory function by employing the thermoresponsive liquid outflow behavior in hydrophobic nanopores. When subjected to heat, the bubble nucleation process is spontaneously activated, and the extent of liquid outflow is promoted. As a result, the system original volume is recovered, and the LN system exhibits an instant volume memory behavior. While in cooling, the gas dissolution process needs one more loading process to trigger and thus the LN system shows a delayed volume memory behavior. A phenomenological constitutive model has also been developed and validated to describe the thermodynamic behavior of the LN-based SMM. Such LN system provides a new paradigm for the design of novel shape memory materials.

Data availability statement

All data that support the findings of this study are included within the article (and any supplementary files).

Acknowledgments

The authors would like to thank the financial support of National Science Foundation (CBET-1803695) and Michigan State University (Startup Grant).

ORCID iDs

Chi Zhan https://orcid.org/0000-0002-7592-7981 Weiyi Lu https://orcid.org/0000-0003-1069-3480

References

- [1] Otsuka K and Wayman C M 1998 Shape Memory Materials (Cambridge: Cambridge University Press)
- [2] Lendlein A and Kelch S 2002 Shape-memory polymers Angew. Chem., Int. Ed. 41 2034–57
- [3] Otsuka K and Ren X 2005 Physical metallurgy of Ti–Ni-based shape memory alloys *Prog. Mater. Sci.* **50** 511–678

- [4] Karaca H E, Saghaian S M, Ded G, Tobe H, Basaran B, Maier H J, Noebe R D and Chumlyakov Y I 2013 Effects of nanoprecipitation on the shape memory and material properties of an Ni-rich NiTiHf high temperature shape memory alloy Acta Mater. 61 7422–31
- [5] Felton S M, Tolley M T, Shin B, Onal C D, Demaine E D, Rus D and Wood R J 2013 Self-folding with shape memory composites Soft Matter 9 7688
- [6] Habault D, Zhang H and Zhao Y 2013 Light-triggered self-healing and shape-memory polymers *Chem. Soc. Rev.* 42 7244
- [7] Michal B T, Jaye C A, Spencer E J and Rowan S J 2013 Inherently photohealable and thermal shape-memory polydisulfide networks ACS Macro Lett. 2 694–9
- [8] Guo W, Lu C-H, Orbach R, Wang F, Qi X-J, Cecconello A, Seliktar D and Willner I 2015 pH-stimulated DNA hydrogels exhibiting shape-memory properties Adv. Mater. 27 73–8
- [9] Han X-J, Dong Z-Q, Fan M-M, Liu Y, Li J H, Wang Y F, Yuan Q J, Li B J and Zhang S 2012 pH-induced shape-memory polymers *Macromol. Rapid Commun.* 33 1055–60
- [10] Sahoo N G, Jung Y C and Cho J W 2007 Electroactive shape memory effect of polyurethane composites filled with carbon nanotubes and conducting polymer *Mater. Manuf. Process.* 22 419–23
- [11] Luo X and Mather P T 2010 Conductive shape memory nanocomposites for high speed electrical actuation Soft Matter 6 2146
- [12] Dunand D C and Müllner P 2011 Size effects on magnetic actuation in Ni-Mn-Ga shape-memory alloys Adv. Mater. 23 216–32
- [13] Mañosa L, González-Alonso D, Planes A, Bonnot E, Barrio M, Tamarit J-L, Aksoy S and Acet M 2010 Giant solid-state barocaloric effect in the Ni–Mn–In magnetic shape-memory alloy *Nat. Mater.* 9 478–81
- [14] Lu H, Gou J, Leng J and Du S 2011 Magnetically aligned carbon nanotube in nanopaper enabled shape-memory nanocomposite for high speed electrical actuation *Appl. Phys. Lett.* 98 174105
- [15] Nespoli A, Besseghini S, Pittaccio S, Villa E and Viscuso S 2010 The high potential of shape memory alloys in developing miniature mechanical devices: a review on shape memory alloy mini-actuators Sensors Actuators A 158 149–60
- [16] Formentini M and Lenci S 2018 An innovative building envelope (kinetic façade) with shape memory alloys used as actuators and sensors *Autom. Constr.* 85 220–31
- [17] Sassa F, Al-Zain Y, Ginoza T, Miyazaki S and Suzuki H 2012 Miniaturized shape memory alloy pumps for stepping microfluidic transport *Sensors Actuators* B 165 157–63
- [18] Cai W, Meng X L and Zhao L C 2005 Recent development of TiNi-based shape memory alloys Curr. Opin. Solid State Mater. Sci. 9 296–302
- [19] Potapova A A and Stolyarov V V 2013 Deformability and structural features of shape memory TiNi alloys processed by rolling with current *Mater. Sci. Eng.* A **579** 114–7
- [20] Liu Y, Du H, Liu L and Leng J 2014 Shape memory polymers and their composites in aerospace applications: a review Smart Mater. Struct. 23 023001
- [21] Behl M, Kratz K, Zotzmann J, Nöchel U and Lendlein A 2013 Reversible bidirectional shape-memory polymers Adv. Mater. 25 4466–9
- [22] Wu J, Lin Y and Sun J 2012 Anisotropic volume change of poly(N-isopropylacrylamide)-based hydrogels with an aligned dual-network microstructure *J. Mater. Chem.* 22 17449–51

- [23] Yang Z, Herd G A, Clarke S M, Tajbakhsh A R, Terentjev E M and Huck W T S 2006 Thermal and UV shape shifting of surface topography J. Am. Chem. Soc. 128 1074–5
- [24] Ortega A M, Yakacki C M, Dixon S A, Likos R, Greenberg A R and Gall K 2012 Effect of crosslinking and long-term storage on the shape-memory behavior of (meth)acrylate-based shape-memory polymers Soft Matter 8 7381
- [25] Pretsch T 2010 Triple-shape properties of a thermoresponsive poly(ester urethane) *Smart Mater. Struct.* **19** 015006
- [26] Zotzmann J, Behl M, Hofmann D and Lendlein A 2010 Reversible triple-shape effect of polymer networks containing polypentadecalactone- and poly(ε-caprolactone)-segments Adv. Mater. 22 3424–9
- [27] Gao Y, Li M, Zhang Y, Lu W and Xu B 2020 Spontaneous outflow efficiency of confined liquid in hydrophobic nanopores *Proc. Natl Acad. Sci.* 117 25246–53
- [28] Zhang Y, Li M, Gao Y, Xu B and Lu W 2018 Compressing liquid nanofoam systems: liquid infiltration or nanopore deformation? *Nanoscale* 10 18444–50
- [29] Li M and Lu W 2017 Liquid marble: a novel liquid nanofoam structure for energy absorption AIP Adv. 7 055312
- [30] Qiao Y, Liu L and Chen X 2009 Pressurized liquid in nanopores: a modified Laplace-Young equation *Nano Lett*.
- [31] Li M and Lu W 2017 Adaptive liquid flow behavior in 3D nanopores *Phys. Chem. Chem. Phys.* **19** 17167–72
- [32] Xu L, Li M and Lu W 2019 Effect of electrolytes on gas oversolubility and liquid outflow from hydrophobic nanochannels *Langmuir* 35 14505–10
- [33] Li M, Xu L and Lu W 2020 Effect of extra gas amount on liquid outflow from hydrophobic nanochannels: enhanced liquid–gas interaction and bubble nucleation *Langmuir* 36 4682–8

- [34] Han A, Kong X and Qiao Y 2006 Pressure induced liquid infiltration in nanopores J. Appl. Phys. 100 014308
- [35] Grosu Y, Ievtushenko O, Eroshenko V, Nedelec J M and Grolier J P E 2014 Water intrusion/extrusion in hydrophobized mesoporous silica gel in a wide temperature range: capillarity, bubble nucleation and line tension effects *Colloids Surf.* A 441 549–55
- [36] Li M, Xu L and Lu W 2019 Nanopore size effect on critical infiltration depth of liquid nanofoam as a reusable energy absorber J. Appl. Phys. 125 044303
- [37] Zhang Y, Li N, Luo R, Zhang Y, Zhou Q and Chen X 2016 Experimental study on thermal effect on infiltration mechanisms of glycerol into ZSM-5 zeolite under cyclic loadings J. Phys. D: Appl. Phys. 49 025303
- [38] Lefevre B, Saugey A, Barrat J L, Bocquet L, Charlaix E, Gobin P F and Vigier G 2004 Intrusion and extrusion of water in hydrophobic mesopores *J. Chem. Phys.* 120 4927–38
- [39] Monnin C, Dubois M, Papaiconomou N and Simonin J-P 2002 Thermodynamics of the LiCl + H₂O System J. Chem. Eng. Data 47 1331-6
- [40] Automotive Electronics Council 2010 AEC-Q200—stress test qualification for passive components pp 1–74
- [41] Coiffard L and Eroshenko V 2006 Temperature effect on water intrusion/expulsion in grafted silica gels J. Colloid Interface Sci. 300 304–9
- [42] Haberland C, Elahinia M, Walker J M, Meier H and Frenzel J 2014 On the development of high quality NiTi shape memory and pseudoelastic parts by additive manufacturing Smart Mater. Struct. 23 104002
- [43] Leo D J 2008 Shape memory alloys Engineering Analysis of Smart Material Systems (Hoboken, NJ: John Wiley & Sons, Inc) pp 298–345